Ultraviolet photodissociation action spectroscopy of gas-phase protonated quinoline and isoquinoline cations

Abstract
The gas-phase photodissociation action spectroscopy of protonated quinoline and isoquinoline cations (quinolineH+ and isoquinolineH+) is investigated at ambient temperature. Both isomers exhibit vibronic detail and wavelength-dependent photoproduct partitioning across two broad bands in the ultraviolet. Photodissociation action spectra are reported spanning 370-285 nm and 250-220 nm and analysed with the aid of electronic structure calculations: TD-DFT (CAM-B3LYP/aug-cc-pVDZ) is used for spectra simulations and CBS-QB3 for dissociation enthalpies. It is shown that the action spectra are afforded predominantly by two-photon excitation. The first band is attributed to both the S1 ← S0 and S2 ← S0 electronic transitions in quinolineH+, with a S1 ← S0 electronic origin assigned at 27 900 cm−1. For isoquinolineH+ the S1 ← S0 transition is observed with an assigned electronic origin at 27 500 cm−1. A separate higher energy band is observed for both species, corresponding to the S3 ← S0 transition, with origins assigned at 42 100 cm−1 and 42 500 cm−1 for quinolineH+ and isoquinolineH+, respectively. Franck-Condon absorption simulations provide an explanation for some vibrational structure observed in both bands allowing several normal mode assignments. The nature of the electronic transitions is discussed and it is shown that the excited states active in the reported spectra should be of $\pi\pi^*$ character with some degree of charge transfer from the homocycle to the heterocycle.

Disciplines
Medicine and Health Sciences | Social and Behavioral Sciences

Publication Details
Hansen, C. S., Blanksby, S. J. & Trevitt, A. J. (2015). Ultraviolet photodissociation action spectroscopy of gas-phase protonated quinoline and isoquinoline cations. Physical Chemistry Chemical Physics, 17 (39), 25882-25890.

Ultraviolet photodissociation action spectroscopy of gas-phase protonated quinoline and isoquinoline cations†

Christopher S. Hansen,[a] Stephen J. Blanksby,[b] and Adam J. Trevitt*[a]

† Electronic Supplementary Information (ESI) available: (1) supplementary mass spectra, (2) isoquinolineH$^+$ molecular orbitals illustrations and (3) optimised quinolineH$^+$/isoquinolineH$^+$ TD-DFT geometries and normal modes. See DOI: 10.1039/C5CP02035B

[a] *School of Chemistry, University of Wollongong, New South Wales 2522, Australia. Fax: +61 2 4221 4287; Tel: +61 2 4221 5455; E-mail: adamt@uow.edu.au*

[b] *Central Analytical Research Facility, Queensland University of Technology, Queensland 4000, Australia*

Abstract

The gas-phase photodissociation action spectroscopy of protonated quinoline and isoquinoline cations (quinolineH$^+$ and isoquinolineH$^+$) is investigated at ambient temperature. Both isomers exhibit vibronic detail and wavelength-dependent photoproduct partitioning across two broad bands in the ultraviolet. Photodissociation action spectra are reported spanning 370 – 285 nm and 250 – 220 nm and analysed with the aid of electronic structure calculations: TD-DFT (CAM-B3LYP/aug-cc-pVDZ) is used for spectra simulations and CBS-QB3 for dissociation enthalpies. It is shown that the action spectra are afforded predominantly by two-photon excitation. The first band is attributed to both the $S_1 \leftarrow S_0$ and $S_2 \leftarrow S_0$ electronic transitions in quinolineH$^+$, with a $S_1 \leftarrow S_0$ electronic origin assigned at 27 900 cm^{-1}. For isoquinolineH$^+$ the $S_1 \leftarrow S_0$ transition is observed with an assigned electronic origin at 27 500 cm^{-1}. A separate higher energy band is observed for both species, corresponding to the $S_3 \leftarrow S_0$ transition, with origins assigned at 42 100 cm^{-1} and 42 500 cm^{-1} for quinolineH$^+$ and isoquinolineH$^+$, respectively. Franck-Condon absorption simulations provide an explanation for some vibrational structure observed in both bands allowing several normal mode assignments. The nature of the electronic transitions is discussed and it is shown that the excited states active in the reported spectra should be of $\pi\pi^*$ character with some degree of charge transfer from the homocycle to the heterocycle.

1 Introduction

Interest in the photochemistry and spectroscopy of polycyclic aromatic nitrogen heterocycles (PANHs) arises in many areas including their purported presence in interstellar media through to their activity in functional materials. There is significant discussion around the proposed role of nitrogen heterocycles in interstellar and extraterrestrial environments. It has been long postulated that polycyclic aromatic hydrocarbons (PAHs) may be responsible for unassigned features (the diffuse interstellar bands, DIBs) in the emission spectrum of the interstellar medium (ISM)[1] and it has been suggested that these bands could indicate the presence of nitrogen heterocycles.[2] Small polycyclic aromatic nitrogen heterocycles (PANHs) like quinoline readily dissociate under exposure to interstellar radiation[3] and there is thus an interest in their photochemistry as they produce reactive photoproducts that may contribute to the composition of the ISM. Furthermore, quinoline and isoquinoline have been detected on meteorites,[4,5] may exist in the atmosphere of Titan[6] and could be involved in the chemical origin of life.[7] Back on Earth, PANHs have been incorporated into functional materials such as organic photovoltaics,[8,9] where there is a clear need to understand their photochemistry and spectroscopy. Ultimately, there is fundamental interest in the electronic spectroscopy of protonated polycyclic aromatic compounds due to their often observed charge-transfer character.[10,11] Quinoline and isoquinoline are shown as their protonated cations, quinolineH$^+$ and isoquinolineH$^+$, in Fig. 1. A significant body of knowledge exists for the electronic spectroscopy of neutral quinolines,[12–14] the quinoline radical cations,[15] and protonated methylquinolines.[16] However, the electronic spectroscopy of isolated protonated quinolines is less reported on.

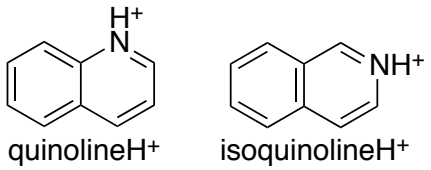

Figure 1: Structures of quinolineH$^+$ and isoquinolineH$^+$.

This manuscript reports the electronic photodissociation action spectroscopy of quinolineH$^+$ and isoquinolineH$^+$ in the gas-phase. Two broad bands exhibiting some vibronic structure are observed in the ultraviolet. One

band spans the region 370 – 285 nm, primarily from the loss of 27 Da (consistent with HCN) and the other band spans 250 – 220 nm and results mostly from the phenylium cation photoproduct (m/z 77). Photoproduct energy calculations also show that, for the most part, at least two photon excitation is required for dissociation of both ions. Time dependent-density functional theory (TD-DFT) calculations assist in the interpretation of these spectra and the features are assigned to the $S_1 \leftarrow S_0$, $S_2 \leftarrow S_0$ and $S_3 \leftarrow S_0$ in quinolineH$^+$ and $S_1 \leftarrow S_0$ and $S_3 \leftarrow S_0$ in isoquinolineH$^+$. The electron density differences, as predicted by the TD-DFT calculations, suggests all bands are of $\pi\pi^*$ character with some evidence for charge transfer from the homocycle to the heterocycle. The laser-power dependence of the photodissociation yield suggests that photodissociation occurs following the absorption of two photons with tentative evidence for a minor single-photon process at higher energies.

2 Methods

2.1 Experimental

The instrumentation and method are described in detail elsewhere[17] and a brief overview is provided here. Photodissociation action spectroscopy experiments were performed using a linear quadrupole ion trap (QIT) mass spectrometer (Thermo Fisher Scientific LTQ) coupled to a tunable laser system. This laser system comprised a midband optical parametric oscillator (OPO) (GWU-Lasertechnik flexiScan) that was pumped by the third harmonic (355 nm) of a 10 Hz, ∼5 ns pulsewidth Nd:YAG laser (Spectra-Physics QuantaRay INDI). This OPO setup is supplied with a frequency conversion unit (GWU-Lasertechnik uvScan) in which ultraviolet light was generated. For the wavelength range 340 – 220 nm, The OPO signal output (visible) was frequency-doubled (second harmonic generation (SHG)). For wavelengths near to the pump photon energy (355 nm), and thus on resonance with the OPO cavity, ultraviolet photons were generated through sum-frequency generation (SFG) using the OPO signal output and the residual light of the Nd:YAG fundamental harmonic (1064 nm). This SFG output was then frequency-doubled to generate ultraviolet photons in the wavelength range 370 – 320 nm and allowing for 20 nm of overlap between the

two harmonic generation methods. Approximately 1 mJ (10 mW @ 10 Hz) of energy was available per SHG pulse and 4-8 mJ per SFG pulse. The PD action spectra are normalised to laser power measured using a Gentec UP17P-6S-W5 power meter. Calibration of the OPO wavelength used a fibre optic pickoff placed before the frequency conversion unit and coupled to a wavelength meter (Toptica HighFinesse WS5). For power dependence studies, the laser power was attenuated using ultraviolet (UV) neutral density filters (Thorlabs NUK01).

Methanolic solutions (10 μM) of quinoline/isoquinoline were introduced into the mass spectrometer by electrospray ionisation (ESI) to generate the gas-phase protonated cations. These cations were transferred into the ion trap, where they are mass-selected and stored. It is expected that the trapped ions become thermalised to near-ambient temperature from collisions with the helium buffer gas (2.5×10^{-3} Torr).[18] Once the target m/z ion population is isolated and stored in the ion trap, a single pulse from the OPO system irradiates the ion cloud along the principle axis. The QIT is then scanned out and a photodissociation mass spectrum is recorded containing photoproduct ion and remaining precursor ion peaks. A photodissociation yield is calculated as the ratio of the photoproduct peak (or peaks) area to the total ion count (TIC). The OPO is then configured to the next wavelength ($\Delta\lambda = 0.1$ nm) and the process repeated. The photoproduct yield is plotted as a function of wavelength to construct the photodissociation action spectrum. The entire process is automated using control software (National Instruments LabVIEW). The PD action spectra reported here are the average of two complete spectra using a wavelength step size of 0.1 nm with ∼80 mass spectra (30 s of acquisition time) averaged at each wavelength. Because isobaric ions were investigated, care was taken to ensure that there was no isomeric contamination of the ESI infusion line, the ESI source interface and the ion optics.

2.2 Computational

The Gaussian 09 software suite was used for all of the electronic structure calculations.[19] TD-DFT[20–26] calculations used the CAM-B3LYP functional[27] and the augmented correlation-consistent polarised double-ζ (aug-cc-PVDZ) basis set.[28–30] CAM-B3LYP with a double-ζ basis set has been shown to be a high-

performing functional for vibronic calculations.[31,32] Franck-Condon absorption spectra were simulated from the unscaled DFT/TD-DFT normal modes and optimised structures using PGOPHER 7.1.[33] Normal modes reported herein are labelled using Mulliken notation. Within each isomer and electronic state, the vibrational modes are grouped by symmetry species and numbered according to their decreasing frequency in ground state quinolineH$^+$. Product energies were calculated using the CBS-QB3 complete basis set method,[34–41] values are reported as the zero-point energy (ZPE)-corrected CBS-QB3 electronic energies.

3 Results and Discussion

3.1 Photodissociation Action Spectroscopy

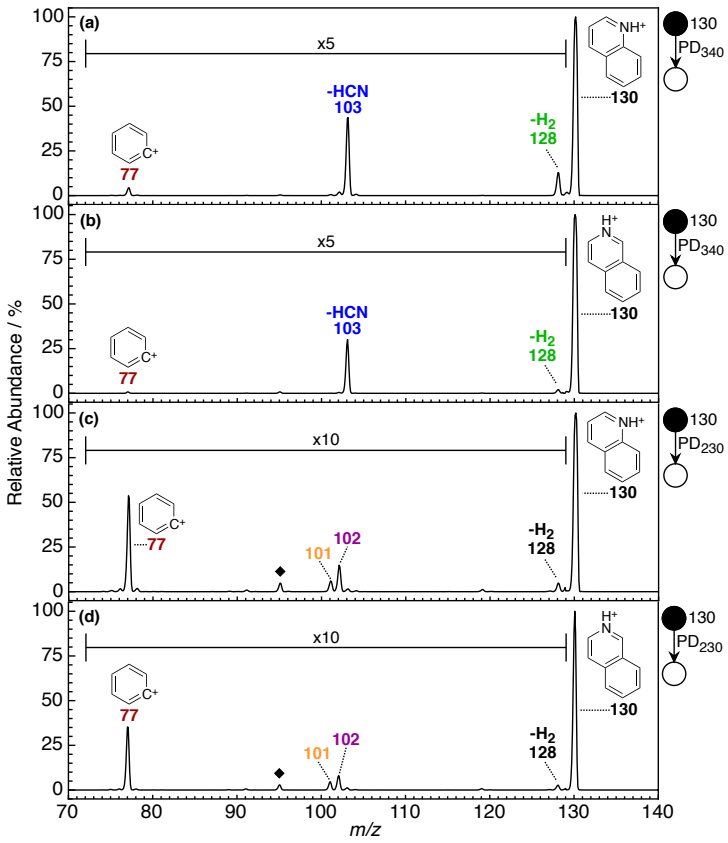

Figure 2: Photodissociation mass spectra of (a) quinolineH$^+$ at λ=340 nm, (b) isoquinolineH$^+$ at λ=340 nm, (c) quinolineH$^+$ at λ=230 nm and (d) isoquinolineH$^+$ at λ=230 nm. Black diamonds indicate the addition of water to the m/z 77 photoproduct.

As will be shown, photodissociation was observed for quinolineH$^+$ and isoquinolineH$^+$ across two dif-

ferent ultraviolet wavelength regions with different PD channels and photoproduct branching fractions. Both species exhibited a *low energy band* between 370 – 285 nm (27 000 – 35 000 cm^{-1}) and the *high energy band* between 250 – 220 nm (40 000 – 45 500 cm^{-1}). Firstly, photodissociation mass spectra are shown for each band in Fig. 2. Fig. 2a shows the photoproducts formed when a mass-selected, trapped population of quinolineH$^+$ cations (*m/z* 130) is irradiated with a 340 nm laser pulse (*i.e.* within the low energy band). The dominant photoproduct occurs at *m/z* 103 and is consistent with the loss of HCN. HCN is a stable, closed-shell neutral species and a familiar coproduct in the photodissociation of nitrogen heterocycles.[42–46] The ion at *m/z* 128 can be rationalised by the loss of molecular hydrogen (H_2). This channel has also been characterised for monocyclic, protonated nitrogen heterocycles and, in those cases, results in a hyperconjugated hetaryne cation.[47,48] Finally, there is a minor photoproduct cation peak visible only under magnification at *m/z* 77. This is assigned to the formation of the phenylium cation and is consistent with the neutral loss of C_3H_3N, which could result from the concerted or sequential loss of HCN and acetylene (HCCH), or from the loss of C_3H_3N as cyclic azete (cyclobutadiene analogue) or linear acrylonitrile (cyanoethylene). The energetics of these photofragmentation pathways are discussed later (section 0.6) and reveal that, in this energy range, at least two photons are required to surmount the product energies. So the dissociation events reported here are almost all afforded by multi-photon dissociation. Laser power dependence experiments are also reported in section 0.6. Clear vibronically resolved two-photon photofragmentation spectra of the protonated indole cation were recently reported by Jouvet and coworkers.[49] Fig. 2b presents the low energy band PD mass spectrum acquired also at $\lambda = 340$ nm for the isoquinolineH$^+$ isomer. The photodissociation yields appear slightly lower in the isoquinolineH$^+$ case, however, the photoproduct *m/z* and partitioning are generally unchanged between the isomers.

High energy band PD mass spectra are shown for $\lambda = 230$ nm for quinolineH$^+$ and isoquinolineH$^+$ in Figs. 2c and 2d, respectively. As for the above case, the photoproduct identities and branching fractions are very similar for both isomers but the yields appear smaller in the isoquinolineH$^+$ case. Across this wavelength range, the dominant charged photoproduct occurs at *m/z* 77. This photoproduct is reactive toward background water (H_2O) in the ion-trap and yields an adduct ion at *m/z* 95, indicated with a

black diamond in Figs. 2c and 2d. The abundance of this m/z 95 ion increases with the storage time of m/z 77 in the ion-trap and when collisionally activated yields primarily m/z 77 (*i.e.* H_2O loss) as well as loss of CO to form a charged product at m/z 67 (see Electronic Supplementary Information section 1). This fragmentation pattern is a signature of protonated phenol, which is known to form in the gas-phase from the reaction of the phenylium cation and water.[50] This supports the assignment of m/z 77 as the phenylium cation. The H_2 loss channel (m/z 128) persists at reduced intensity in the high energy band of both isomers and minor products are also visible under magnification at m/z 102 and 101. These minor photoproduct ions at m/z 102 and 101 have not been studied in detail here and are consistent with the neutral loss of acetylene (28 Da) from from the precursor ion (m/z 130) and the loss of HCN (27 Da) from the -H_2 photoproduct (m/z 128), respectively.

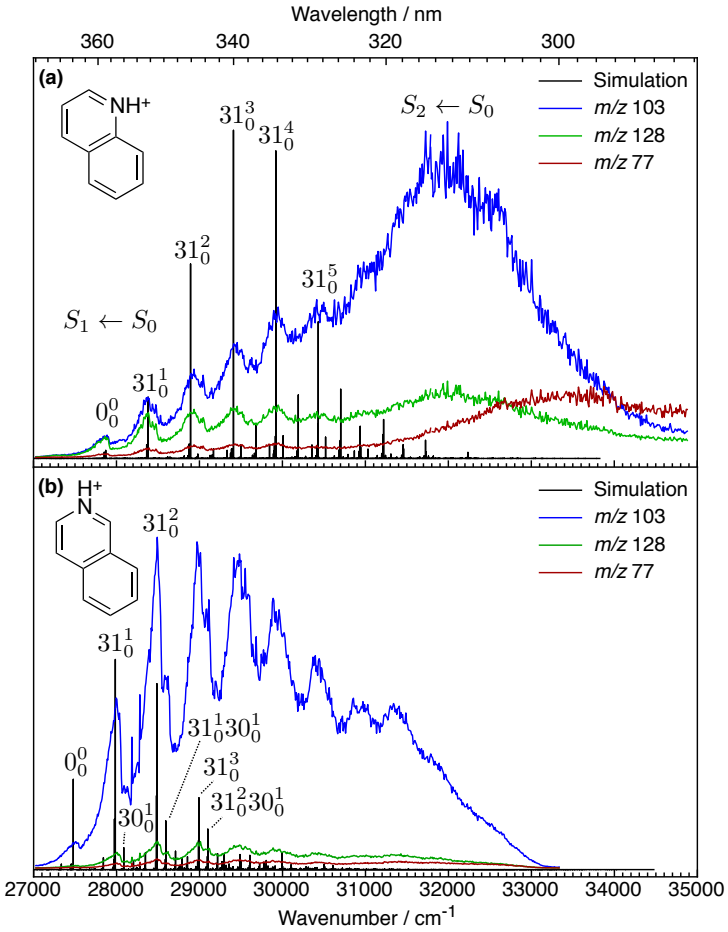

Figure 3: Photodissociation action spectra of the low energy bands (370 – 285 nm) of (a) quinolineH$^+$ and (b) isoquinolineH$^+$. Each spectra is compared to an annotated simulation described in the text.

Photodissociation action spectra were measured for the low and high energy UV bands of quinolineH$^+$

and isoquinolineH$^+$ by recording PD mass spectra, such as those shown in Fig. 2, across each broad wavelength range at $\Delta\lambda = 0.1$ nm. Because the PD action spectra are constructed from mass spectra, every product channel is recorded for each laser pulse. These PD action spectra are presented for the low energy band in Fig. 3 and for the high energy band in Fig. 4. The assignments and annotations are described later in section 0.4. When examining the *m/z* 103 channel in Fig. 3a (blue), the 370 – 280 nm band of quinolineH$^+$ begins with a gradual onset to a low-intensity, broad feature that peaks at around 27 900 cm^{-1}. This peak leads a progression with a repeated spacing of ∼500 cm^{-1}. These features become less prominent as a broad, structureless and intense feature (centred at 32 000 cm^{-1}) eventually dominates. Initially, the other two plotted PD fragmentation (*m/z* 128 and 77) channels follow the same trends at lower intensities. Interestingly, the *m/z* 77 (dark red) channel exhibits a more gradual onset for the dominant broad feature and eventually equals the maximum intensity of and outcompetes the H_2-loss channel (green). By 290 nm, *m/z* 77 becomes the dominant photoproduct channel.

For isoquinolineH$^+$ (Fig. 3b), the *m/z* 103 channel is the most intense and also displays some vibronic detail. This signal exhibits a gradual onset to a low-intensity feature centred around 27 500 cm^{-1}, about 400 cm^{-1} lower in energy than the first feature in the quinolineH$^+$ spectrum. As in the quinolineH$^+$ case, this feature begins a progression with at least eight more peaks occurring roughly every 500 cm^{-1}. Many of these features also appear to have a shoulder feature approximately 100 cm^{-1} higher in energy. In contrast to the quinolineH$^+$ spectrum in Fig. 3a, the structureless dominant feature is absent in the isoquinolineH$^+$ spectrum and the low energy band returns to its baseline by 300 nm (33 000 cm^{-1}).

The PD action spectrum for the high energy band of quinolineH$^+$ is shown in Fig. 4a. The dominant *m/z* 77 channel is plotted alongside the *m/z* 102 and 101 channels. These PD fragmentation channels all track similarly with no λ-dependent partitioning; the *m/z* 77:102:101 relative branching fraction is 73 ± 4:19 ± 3:8 ± 1 ($\pm 2\sigma$) across this wavelength range. Each channel gradually onsets to a broad feature centred around 42 100 cm^{-1} that is well-resolved from the remainder of the band. The high energy band in isoquinolineH$^+$, Fig. 4b, observes a *m/z* 77:102:101 relative branching fraction of 74 ± 3:16 ± 2:9 ± 1 ($\pm 2\sigma$). Compared to the quinolineH$^+$ spectrum in Fig. 4a, it shows similar wavelength-dependent photodissociation

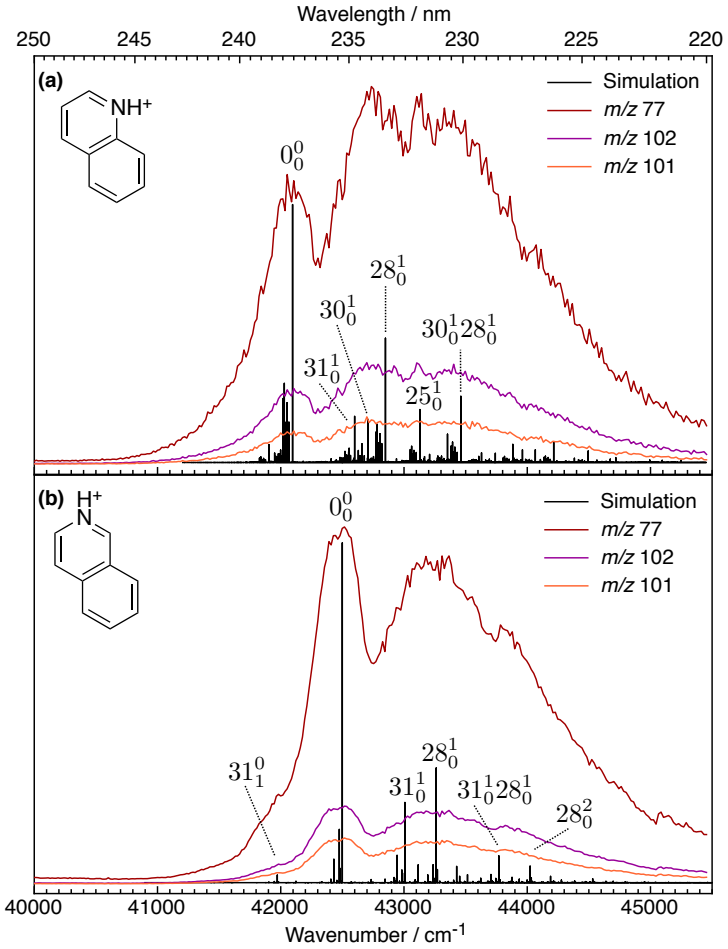

Figure 4: Photodissociation action spectra of the high energy bands (250 – 220 nm) of (a) quinolineH$^+$ and (b) isoquinolineH$^+$. The comparison to a simulation and the assignments are described in the text.

and is slightly red-shifted – the first feature is centred around 42 500 cm^{-1}.

3.2 Spectral Analysis

The TD-DFT model used to simulate the experimental spectra predicted the first five low-lying singlet electronic transitions to have non-zero vertical oscillator strengths for both isomers. These transitions all involve rearrangement and localisation of the π electrons. The orbitals involved in the three lowest lying transitions of quinolineH$^+$ are presented graphically in Fig. 5 as isodensity surfaces representing the volume where the probability of finding an electron is $\geq 98\%$. The equivalent isoquinolineH$^+$ MOs appear in the Electronic Supplementary Information section 2. The two ground-state occupied orbitals in Fig. 5 are all bonding π-type molecular orbitals and include the highest occupied molecular orbital (HOMO) and the second highest (HOMO-1). The ground-state unoccupied orbitals shown in Fig. 5 include the

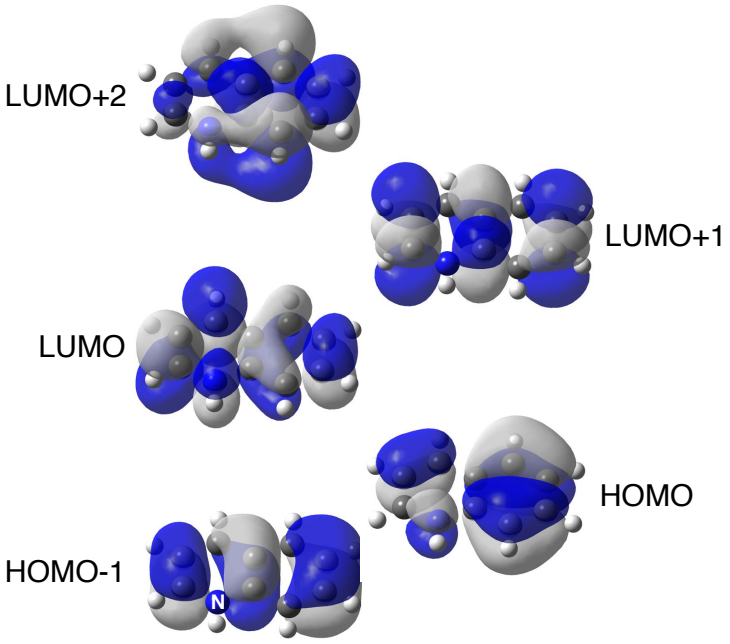

Figure 5: Valence molecular orbitals active in the lowest three electronic transitions of quinolineH$^+$.

three lowest unoccupied molecular orbitals (LUMO, LUMO+1 and LUMO+2). On comparison with the occupied orbitals in Fig. 5, each of these unoccupied MOs represents a more localised π electron system.

Table 1: The three lowest-lying, predicted electronic transitions in quinolineH$^+$.

	Adiabatic / Vertical Transition Energy / cm^{-1}	Oscillator Strength	Configuration State	%
S_1	29 971 / 32 479	0.0401	HOMO $\rightarrow$ LUMO	95
			HOMO-1 $\rightarrow$ LUMO+1	2
S_2	35 737 / 36 164	0.0967	HOMO-1 $\rightarrow$ LUMO	76
			HOMO $\rightarrow$ LUMO+1	22
S_3	46 247 / 47 091	0.6386	HOMO $\rightarrow$ LUMO+1	63
			HOMO-1 $\rightarrow$ LUMO	20
			HOMO-1 $\rightarrow$ LUMO+2	13

For quinolineH$^+$, the predicted adiabatic and vertical transition energies and oscillator strengths are tabulated alongside the contribution of each configuration state in Table 1. The first transition is dominated by a HOMO to LUMO transition and is expected to have an adiabatic excitation energy of 29 971 cm^{-1}, about 2000 cm^{-1} higher in energy than the first feature in low energy band PD action spectrum, Fig. 3a. A Franck-Condon absorption spectrum into this electronic state was simulated using the unscaled TD-DFT results and PGOPHER 7.1. The most active normal modes in the vibronic spectra were found to all be in-plane (a') ring deformations, a familiar result in aromatic electronic spectroscopy. These normal modes are shown schematically in Fig. 6. The simulated spectrum for the $S_1 \leftarrow S_0$ transition is overlaid upon the

experimental low energy band spectra in Fig. 3a. The simulated spectrum has been linearly red-shifted by 2071 cm-1 from the predicted TD-DFT origin value and shows good agreement between the predicted spacing of prominent vibronic features. A progression in the ν_{31} (a') mode is the most pronounced feature of the simulation can account for the 500 cm^{-1} progression that provides most of the detail in the lowest energy half of this band. The predicted TD-DFT frequency for this mode (refer Electronic Supplementary Information section 3) is 513 cm^{-1} and in close accord with the measured spacing. Within this model, the electronic origin (0_0^0), *i.e.* the adiabatic transition energy, has been assigned as 27 900 cm^{-1}. Based on the width of the broad peaks, the determination of the origins transitions are assigned an uncertainty of ∼50 cm^{-1}.

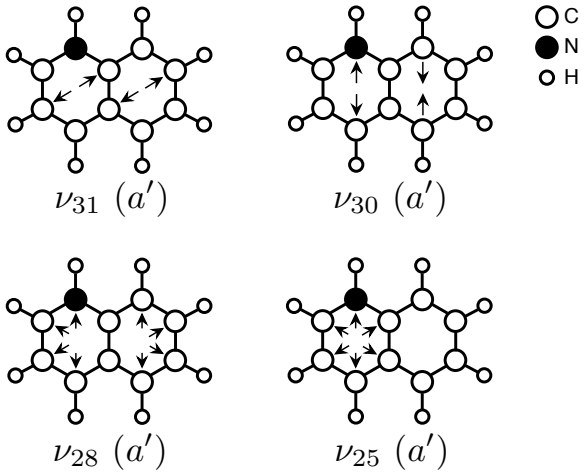

Figure 6: Schematic representation of the important quinolineH$^+$ normal modes referred to in text and used in vibronic assignments. The arrows indicate the direction of motion and are not proportional in length to the magnitude. The normal modes in isoquinolineH$^+$ are analogous

Although the band spacings predicted by TD-DFT appear reasonable, the simulated and measured spectral intensities do not agree. The intensity profile of the absorption spectrum may be modulated significantly by dissociation processes. It has been shown for the pyridineH$^+$ cation, from which quinolineH$^+$ and isoquinolineH$^+$ are derived, that the dominant features and band spacings are conserved between photodissociation and rare gas tagging measurements but the PD action spectrum signal increases with photon energy (*i.e.* shorter wavelengths) and is raised off the baseline with a broad envelope.[47]

The intense broad and unfeatured band centred around 32 000 cm^{-1} is not predicted by this simulation.

Table 1 lists a second electronic transition, to S_2, with a vertical excitation energy approximately 3500 cm^{-1} higher than that to S_1. The oscillator strength is also expected to be about 2.5x greater for this $S_2 \leftarrow S_0$ transition. These two predicted properties support the assignment of the broad feature in Fig. 3a as the $S_2 \leftarrow S_0$ transition. Although the S_2 electronic state optimised to a bound geometry, this broad feature displays no finer details. This suggests that there might be dynamical differences between the deactivation of the S_1 and S_2 electronic states. As there were no finer details resolved in the experiment, the FC absorption spectrum was not simulated for this transition.

Table 2: The three lowest-lying, predicted electronic transitions in isoquinolineH$^+$.

	Adiabatic / Vertical Transition Energy / cm^{-1}	Oscillator Strength	Configuration State	%
S_1	29 955 / 32 038	0.0699	HOMO $\rightarrow$ LUMO	95
			HOMO-1 $\rightarrow$ LUMO+1	4
S_2	37 052 / 38 049	0.0011	HOMO $\rightarrow$ LUMO+1	51
			HOMO-1 $\rightarrow$ LUMO	46
S_3	46 494 / 47 317	0.7135	HOMO-1 $\rightarrow$ LUMO	48
			HOMO $\rightarrow$ LUMO+1	36
			HOMO $\rightarrow$ LUMO+2	6
			HOMO $\rightarrow$ LUMO+1	5

Turning now to the low energy band of isoquinolineH$^+$, its three lowest-lying, predicted electronic transitions are tabulated in Table 2. Each of these transitions in isoquinolineH$^+$ comprises the same dominant configuration states and ordering as quinolineH$^+$, albeit with minor variations in CI wavefunction contributions. The first electronic transition, $S_1 \leftarrow S_0$, is predicted to involve primarily the HOMO $\rightarrow$ LUMO excitation with adiabatic and vertical transition energies of 29 955 and 32 038 cm^{-1}, respectively. These energies are lower than those predicted for quinolineH$^+$, in accord with the observed red shift discussed above. For these ions, the TD-DFT method predicted relative energies in accord with the experimental results, however, the absolute energies were less accurate. The calculated oscillator strength for the $S_2 \leftarrow S_0$ transition in isoquinolineH$^+$ (0.0011) is an order of magnitude lower than that of the $S_1 \leftarrow S_0$ transition (0.0699). This provides further support for the above assignment and also demonstrates a case where a pronounced spectral feature can be switched off by a minor structural perturbation. Exchanging a protonated aryl nitrogen and a sp^2 carbon leads to an isoelectronic ion. This significant difference in both photoproduct abundance and partitioning presents a structurally-diagnostic measurement that could

be used to identify isomers of protonated quinoline – particularly around 300 nm.

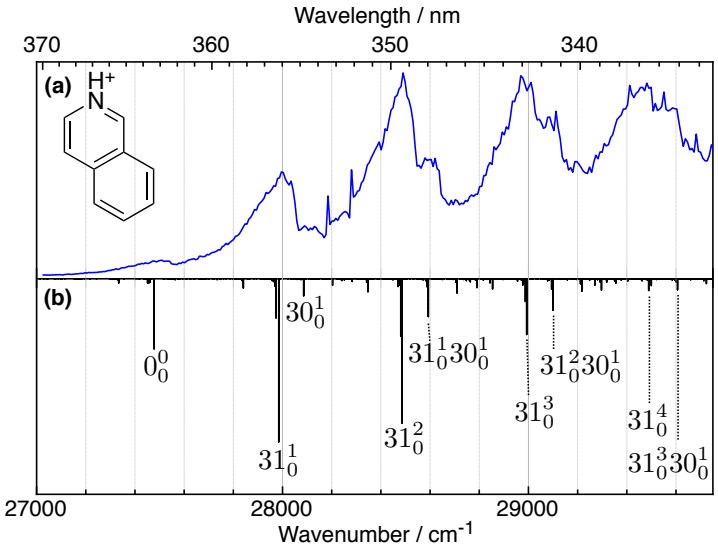

Figure 7: (a) Magnified (370 – 330 nm) photodissociation action spectrum (m/z 77) of the isoquinolineH$^+$ low energy band around the onset and first four quanta of excitation in the main progression compared to the (b) Franck-Condon absorption spectrum simulation. The assignments and simulation are explained in the text.

The vibronic FC absorption spectrum was also simulated for the $S_1 \leftarrow S_0$ transition in isoquinolineH$^+$. This simulation was red-shifted 2455 cm^{-1} and plotted with the experimental measurement in Fig. 3b. The low energy part of this simulation is magnified in Fig. 7. The experimental line spacings are reproduced by a progression in the ν_{31} (a') normal mode (see Fig. 6). The unscaled predicted frequency for this mode is 506 cm^{-1} (see Electronic Supplementary Information section 3) and in close agreement with the measured frequency of 500 cm^{-1}. The small features that accompany the high-energy shoulder of many of these peaks line up with the simulated $31_0^n 30_0^1$ progression to which they are assigned in Fig. 3b. The experimentally determined frequency of the ν_{30} (a') mode is thus approximately 600 cm^{-1} and well-predicted by TD-DFT as 612 cm^{-1}. The electronic origin (0_0^0) has been assigned as 27 500 cm^{-1}.

Because the TD-DFT method yielded a simple description of the two lowest-lying excited states that could be used to recreate and understand the experimental low energy band, a similar attempt was made for the $S_3 \leftarrow S_0$ transition. The adiabatic/vertical transition energies in Tables 1 & 2 are predicted to be 46 247/47 091 cm^{-1} (quinolineH$^+$) and 46 494/47 317 cm^{-1} (isoquinolineH$^+$), overestimated again by several thousand wavenumbers compared to the measured spectra in Figs. 4a & 4b. The isoquinolineH$^+$

band is expected to occur 226 cm^{-1} higher in energy and is indeed visibly blue-shifted in Fig. 4.

The FC absorption spectrum simulations are shown overlaying the experimental spectra in Fig. 4. These simulations were shifted 4147 cm^{-1} (quinolineH$^+$) and 3994 cm^{-1} (isoquinolineH$^+$) lower in energy from the predicted TD-DFT origin values and are also dominated by the in-plane ring deformations illustrated in Fig. 6. Both spectra are characterised by the first intense feature appearing as a pronounced peak that is separated from the remainder of the congested vibronic transitions. From the simulation this can be assigned as the electronic origin transition (0_0^0) occurring around 42 100 cm^{-1} in quinolineH$^+$ and 42 500 cm^{-1} in isoquinolineH$^+$. This difference in origin energies is 153 cm^{-1} greater ($\sim$1.6$\times$) than that predicted by CAM-B3LYP/aug-cc-pVDZ. The simulation also predicts a ν_{31} (a') hot band lying 526 cm^{-1} lower in energy than the electronic origin. This simulated vibronic transition lines up with a bump in the onset of the experimental spectrum. However, it is not well-resolved. The ground state frequency of this normal mode has been determined experimentally as 521 cm^{-1},[51] which is close to the predicted 526 cm^{-1}, showing that the TD-DFT method can provide good estimates for vibrational spacing in both the ground and excited electronic states.

3.3 Discussion of the Electronic States

It has been recently reported that electronic transitions of protonated polycyclic aromatic hydrocarbons often possess a strong charge-transfer character – especially when the system has an even number of rings.[10] When exploring the character of an excited state, it is helpful to examine the differences between the excited and ground state electronic densities. These are shown in Fig. 8 for the three lowest-lying excited states of both isomers. These surfaces represent the subtraction of the ground state DFT density from an excited state electronic density where grey indicates a volume of decreased density and blue of increased density. The $S_1 \leftarrow S_0$ transitions in quinolineH$^+$ (Fig. 8a) and isoquinolineH$^+$ (Fig. 8d) are almost singlet HOMO $\rightarrow$ LUMO transitions. On examining the HOMO and LUMO molecular orbitals in Fig 5 it is expected that this transition will involve localisation of the π electrons and, perhaps, the transfer of charge from the homocycle to the heterocycle. This is represented graphically in Figs. 8a & 8d. There are large volumes

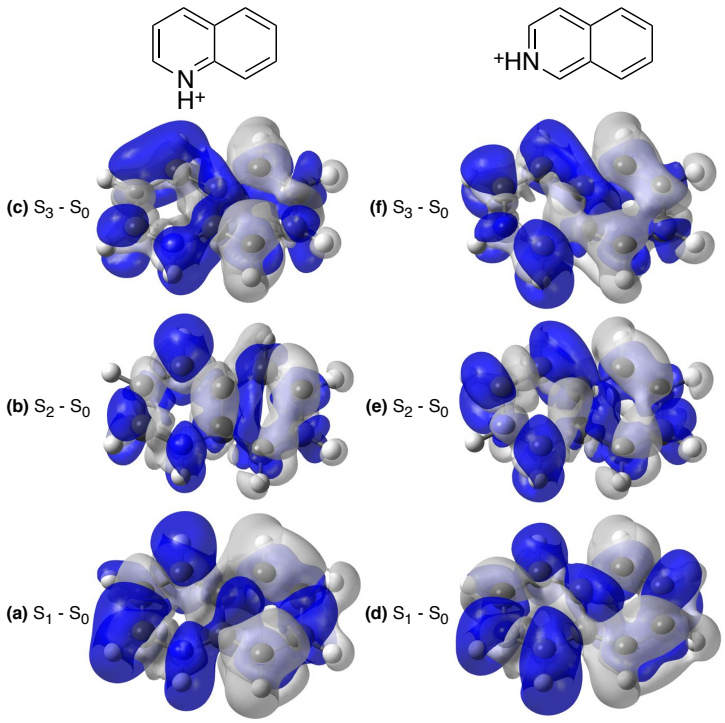

Figure 8: Electronic probability density differences between the first three excited states and the ground state of quinolineH$^+$ (a-c) and isoquinolineH$^+$ (d-f).

of blue π density on the nuclei and grey volume surrounding the chemical bonds. Comparing over the two rings, a small degree of charge transfer from the heterocycle to homocycle is perhaps evident. The first excited state, in both cases, involves primarily the transformation from a π bonding to a π anti-bonding arrangement ($\pi\pi^*$) with some charge-transfer. The second singlet electronic transition ($S_2 \leftarrow S_0$) is more complex and is controlled, for each isomer, by two dominant excitations in either a 2:1 (quinolineH$^+$) or 1:1 (isoquinolineH$^+$) ratio (Tables 1 & 2). The consequences of these rearrangements on the electronic densities are visualised in Figs. 8b & 8e. This electronic state also exhibits π^* character that can be observed from the movement of π electron density from the bonds to the nuclei. It also involves a greater degree of localisation of the π electrons on particular nuclei. Significant charge transfer character is not as clear for this excited state. The S_3 - S_0 electronic density difference is shown for both isomers in Figs. 8c & 8f. This electronic state also results from a multiplet excitation (Tables 1 & 2) but the movement of electrons can be characterised from the density differences in Fig. 8. This transition involves some redistribution of electronic density from the homocycle to the heterocycle.

3.4 Product Channels

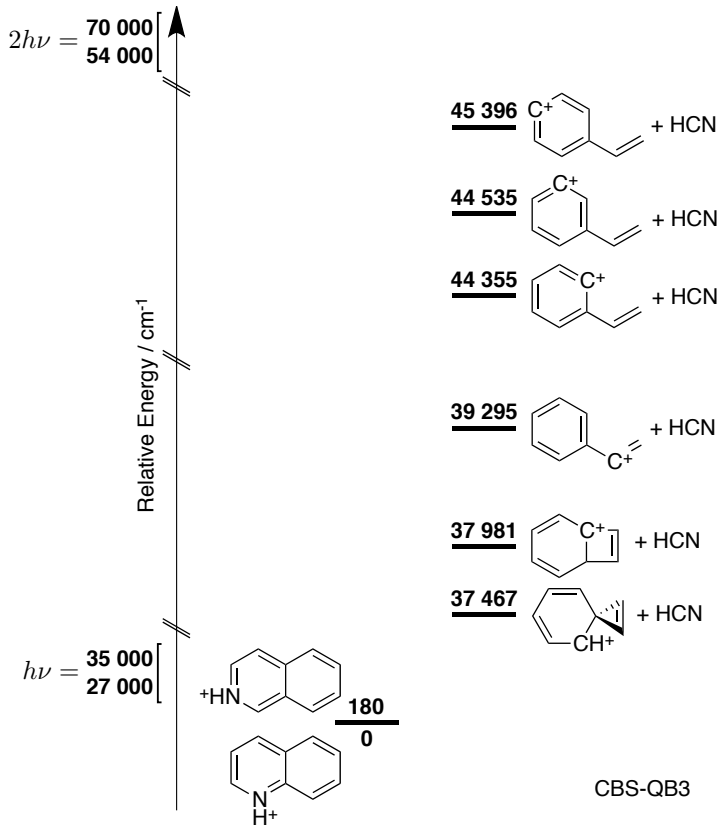

Figure 9: CBS-QB3 enthalpies (in wavenumbers) for the six channels for the ground-state HCN loss from quinolineH$^+$ and the isomerisation to isoquinolineH$^+$. The single- and two-photon energy ranges are labelled on the vertical axis.

For the low energy band, where HCN loss is dominant, the enthalpies of six photoproduct channels have been calculated using the CBS-QB3 method, shown in Fig. 9. The bicyclic photoproducts are resonance stabilised and reside between 37 000 and 38 000 cm^{-1}. The styrene derivative cations lie higher in energy: when the aromatic phenyl ring remains intact, this channel requires more than 39 000 cm^{-1} of energy and when a carbocation is incorporated in the ring ∼45 000 cm^{-1} is required. We note that the CBS-QB3 method optimises the styrene derivative with a terminal carbocation, (phenyl)-CH=CH$^+$, to the lowest energy bicyclic structure shown in Fig. 9. The single-photon ($h\nu$) and two-photon ($2h\nu$) energy ranges are labelled on the vertical axis and bracket all of the photoproduct channel enthalpies. The lowest energy product channel requires energy about 7 500 cm^{-1} greater than that of the most energetic low energy band photon while the highest energy channel is more than 3 500 cm^{-1} below the two-photon energy range. The low energy band cannot be the result of single photon dissociation. Two photons however, exceed the

relative enthalpies of all photoproduct channels located.

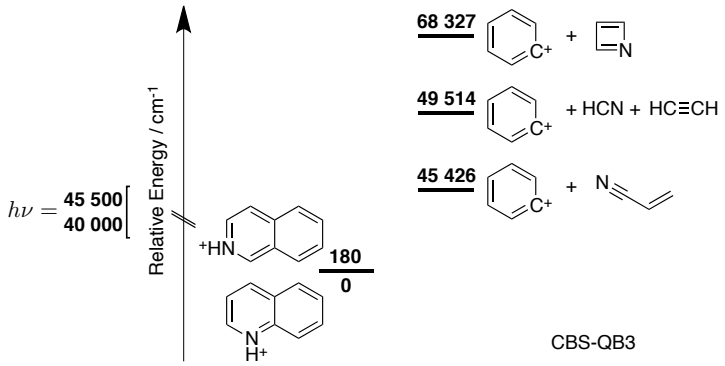

Figure 10: CBS-QB3 enthalpies (in wavenumbers) for the ground-state formation of the phenylium cation from quinolineH$^+$ and the isomerisation to isoquinolineH$^+$. The single-photon energy range is labelled on the vertical axis.

The scenario is similar for the high energy band. The calculated energies required to form the *m/z* 77 phenylium cation and three possible coproduct channels – acrylonitrile, HCN+acetylene and azete – are shown in Fig. 10. Once again, most of the experimental photon energies are below the product enthalpies of the photoproduct channels. However, the enthalpy of the phenylium + acrylonitrile channel lies within the upper end of this band, albeit where there is a little spectral activity, see Figs. 4a & 4b. A more complete energy surface would be required to better predict which $C_8H_7^+$ isomer forms.

Power dependence measurements of photofragmenation can provide insight into the absorption process. The absorption of an ion population, A, will vary according to the intensity of the input light (*i.e.* the laser power), I, according to the relationship[52]

$$A \propto \sigma_1 I + \sigma_2 I^2 + \sigma_3 I^3 + \ldots \tag{1}$$

where σ_1 is the linear absorption cross-section, σ_2 the two-photon absorption cross section, and so on. Thus, if one process is dominant, the response of absorption (and therefore photodissociation) to laser power will be either linear, quadratic, cubic, *et cetera*, depending on the number of photons involved.

This was explored for the formation of *m/z* 103 (HCN loss) from quinolineH$^+$ within the low energy band wavelength range. Figs. 11a-c plot the yield of this photoproduct at different laser powers at $\lambda =$ (a) 320 nm (b), 310 nm and (c) 300 nm. Each of these curves can be described by a fitted quadratic

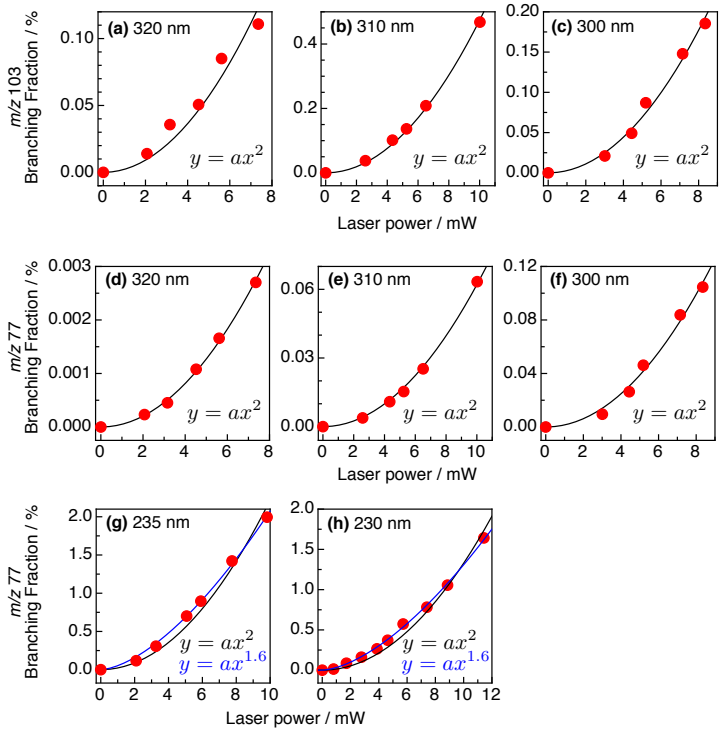

Figure 11: Laser-power dependence of the (a-c) quinolineH$^+$ m/z 103 photoproduct yield within the low energy band and the m/z 77 photoproduct yield across the (d-f) low energy and (g,h) high energy bands.

function of the form $y = ax^2$. This suggests that, throughout this band, the formation of HCN and m/z 103 proceeds the absorption of two photons. To examine the change in photoproduct branching ratio that occurs around the assigned $S_2 \leftarrow S_0$ transition, and explore if a new process becomes available, these data are plotted for the m/z 77 channel in Figs. 11d-f. The points λ = (d) 320 nm (e), 310 nm and (f) 300 nm occur before, during and after the point of inflection in the m/z 77 photoproduct action spectrum (Fig. 3a), respectively. At each wavelength, the m/z 77 branching fraction observes a quadratic dependence on laser power and dominated by two photon excitation. Within the low energy band, m/z 103 & 77 are formed from a two-photon process. The λ-dependent photoproduct partitioning may then be the result of different pathways leading to photodissociation. Figs. 11g-h graph the appearance of m/z 77 against laser power at two different points within the high energy band: (g) 235 nm and (h) 230 nm. The power-dependencies are not as well-described by an optimised quadratic function as those for the low energy band. Instead, the response to laser power is better represented by a power function $y = ax^{1.6}$. This suggests that photodissociation within this band may be accessible with a single photon yet still occurs

dominantly by a two-photon process.

4 Conclusions

The electronic photodissociation action spectroscopy has been recorded, in the gas-phase, for quinolineH$^+$ and isoquinolineH$^+$. This dataset expands the library of existing knowledge to include the protonated quinoline spectra amongst that of neutral, substituted and radical cation quinoline derivatives. It is shown that both isomers contain two broad, vibronically-structured bands in their electronic spectra with a wavelength-dependence of the photoproduct branching fractions. The low energy band spans 370 – 285 nm and is dominated by a photodissociation mass channel consistent with HCN (27 Da) loss. The high energy band spans 250 – 220 nm and the measured signal arises primarily from the detection of the phenylium cation ($C_6H_5^+$). The low energy band is assigned to the two closely-lying $S_1 \leftarrow S_0$ and $S_2 \leftarrow S_0$ transitions in quinolineH$^+$, and to the $S_1 \leftarrow S_0$ transition in isoquinolineH$^+$. The spectra are most different, in both intensity and photoproduct partitioning, across the region 310 – 300 nm, presenting a possible structurally-diagnostic measurement that could be used to identify either protonated quinoline isomer amongst a *m/z* 130 ion population. The S_1 electronic origins have been measured to be 27 900 cm^{-1} and 27 500 cm^{-1} for quinolineH$^+$ and isoquinolineH$^+$, respectively. The S_1 state vibrational frequency of the ν_{31} (a') mode has been measured to be approximately 500 cm^{-1} for both isomers and harmonic at up to five and eight quanta of excitation in quinolineH$^+$ and isoquinolineH$^+$, respectively. The experimental frequency for the ν_{30} (a') normal mode in isoquinolineH$^+$ is about 600 cm^{-1}. The high energy band has assigned electronic origins at 42 100 cm^{-1} (quinolineH$^+$) and 42 500 cm^{-1} (isoquinolineH$^+$), exhibits little resolvable structure and is attributed, in both cases, to the $S_3 \leftarrow S_0$ transition. Finally, due to the broad spectral features in the action spectra, the accuracy of electronic origin determinations are likely to be significantly improved with colder ions.

5 Acknowledgements

Financial support for this project was provided by the Australian Research Council (ARC) Grants: CE0561607, DP120102922, DP140101237. This research was undertaken with the assistance of resources provided at the NCI National Facility systems at the Australian National University through the National Computational Merit Allocation Scheme supported by the Australian Government. Computational (and/or storage) resources used in this work were also provided by Intersect Australia Ltd.

References

[1] A. Tielens, *Ann. Rev. Astron. Astrophys.*, 2008, **46**, 289–337.

[2] D. M. Hudgins, J. Charles W. Bauschlicher and L. J. Allamandola, *Astrophys. J.*, 2005, **632**, 316.

[3] A. G. G. M. Tielens, *Rev. Mod. Phys.*, 2013, **85**, 1021–1081.

[4] P. G. Stoks and A. W. Schwartz, *Geochim. Cosmochim. Acta*, 1982, **46**, 309–315.

[5] P. G. Stoks and A. W. Schwartz, *Geochim. Cosmochim. Acta*, 1981, **44**, 563–569.

[6] A. Landera and A. M. Mebel, *Faraday Discuss.*, 2010, **147**, 479–494.

[7] Z. Peeters, O. Botta, S. B. Charnley, Z. Kisiel, Y.-J. Kuan and P. Ehrenfreund, *Astronomy Astrophys.*, 2005, **433**, 583–590.

[8] J.-Y. Li, C.-Y. Chen, W.-C. Ho, S.-H. Chen and C.-G. Wu, *Organic Letters*, 2012, **14**, 5420–5423.

[9] J. Zhao, X. Yang, M. Cheng, S. Li, X. Wang and L. Sun, *J. Mater. Chem. A*, 2013, **1**, 2441–2446.

[10] I. Alata, C. Dedonder, M. Broquier, E. Marceca and C. Jouvet, *J. Am. Chem. Soc.*, 2010, **132**, 17483–17489.

[11] S. Chakraborty, R. Omidyan, I. Alata, I. B. Nielsen, C. Dedonder, M. Broquier and C. Jouvet, *J. Am. Chem. Soc.*, 2009, **131**, 11091–11097.

[12] A. Hiraya, Y. Achiba, K. Kimura and E. Lim, *Chem. Phys. Lett.*, 1991, **185**, 303 – 309.

[13] J. Wanna and E. R. Bernstein, *J. Chem. Phys*, 1987, **86**, 6707–6716.

[14] J. Bouwman, B. Sztaray, J. Oomens, P. Hemberger and A. Bodi, *J. Phys. Chem. A*, 2015, **119**, 1127–1136.

[15] V. Dryza, J. A. Sanelli, E. G. Robertson and E. J. Bieske, *J. Phys. Chem. A*, 2012, **116**, 4323–4329.

[16] Klærke, B., Holm, A. I. S. and Andersen, L. H., *Astron. Astrophys.*, 2011, **532**, A132.

[17] C. S. Hansen, B. B. Kirk, S. J. Blanksby, R. A. J. O'Hair and A. J. Trevitt, *J. Am. Soc. Mass Spectrom.*, 2013, **24**, 932–940.

[18] D. G. Harman and S. J. Blanksby, *Org. Biomol. Chem.*, 2007, **5**, 3495–3503.

[19] M. J. Frisch, G. W. Trucks, H. B. Schlegel, G. E. Scuseria, M. A. Robb, J. R. Cheeseman, G. Scalmani, V. Barone, B. Mennucci, G. A. Petersson, H. Nakatsuji, M. Caricato, X. Li, H. P. Hratchian, A. F. Izmaylov, J. Bloino, G. Zheng, J. L. Sonnenberg, M. Hada, M. Ehara, K. Toyota, R. Fukuda, J. Hasegawa, M. Ishida, T. Nakajima, Y. Honda, O. Kitao, H. Nakai, T. Vreven, J. A. Montgomery, Jr., J. E. Peralta, F. Ogliaro, M. Bearpark, J. J. Heyd, E. Brothers, K. N. Kudin, V. N. Staroverov, R. Kobayashi, J. Normand, K. Raghavachari, A. Rendell, J. C. Burant, S. S. Iyengar, J. Tomasi, M. Cossi, N. Rega, J. M. Millam, M. Klene, J. E. Knox, J. B. Cross, V. Bakken, C. Adamo, J. Jaramillo, R. Gomperts, R. E. Stratmann, O. Yazyev, A. J. Austin, R. Cammi, C. Pomelli, J. W. Ochterski, R. L. Martin, K. Morokuma, V. G. Zakrzewski, G. A. Voth, P. Salvador, J. J. Dannenberg, S. Dapprich, A. D. Daniels, O. Farkas, J. B. Foresman, J. V. Ortiz, J. Cioslowski and D. J. Fox, *Gaussian∼09 Revision D.01*, Gaussian Inc. Wallingford CT 2009.

[20] G. Scalmani, M. Frisch, B. Mennucci, J. Tomasi, R. Cammi and V. Barone, *J. Chem. Phys.*, 2006, **124**, 094107.

[21] F. Furche and R. Ahlrichs, *J. Chem. Phys.*, 2002, **117**, 7433–7447.

[22] C. Van Caillie and R. Amos, *Chem. Phys. Lett.*, 2000, **317**, 159–164.

[23] C. Van Caillie and R. Amos, *Chem. Phys. Lett.*, 1999, **308**, 249–255.

[24] R. Stratmann, G. Scuseria and M. Frisch, *J. Chem. Phys.*, 1998, **109**, 8218–8224.

[25] M. Casida, C. Jamorski, K. Casida and D. Salahub, *J. Chem. Phys.*, 1998, **108**, 4439–4449.

[26] R. Bauernschmitt and R. Ahlrichs, *Chem. Phys. Lett.*, 1996, **256**, 454–464.

[27] T. Yanai, D. Tew and N. Handy, *Chem. Phys. Lett.*, 2004, **393**, 51–57.

[28] D. Woon and T. Dunning, *J. Chem. Phys.*, 1993, **98**, 1358–1371.

[29] R. Kendall, T. Dunning and R. Harrison, *J. Chem. Phys.*, 1992, **96**, 6796–6806.

[30] T. Dunning, *J. Chem. Phys.*, 1989, **90**, 1007–1023.

[31] G. V. Lopez, C.-H. Chang, P. M. Johnson, G. E. Hall, T. J. Sears, B. Markiewicz, M. Milan and A. Teslja, *J. Phys. Chem. A*, 2012, **116**, 6750–6758.

[32] I. M. Alecu, J. Zheng, Y. Zhao and D. G. Truhlar, *J. Chem. Theory Comput.*, 2010, **6**, 2872–2887.

[33] *PGOPHER, a Program for Simulating Rotational Structure, C. M. Western, University of Bristol, http://pgopher.chm.bris.ac.uk*, 2010.

[34] J. Montgomery, M. Frisch, J. Ochterski and G. Petersson, *J. Chem. Phys.*, 2000, **112**, 6532–6542.

[35] J. Montgomery, M. Frisch, J. Ochterski and G. Petersson, *J. Chem. Phys.*, 1999, **110**, 2822–2827.

[36] J. Ochterski, G. Petersson and J. Montgomery, *J. Chem. Phys.*, 1996, **104**, 2598–2619.

[37] J. Montgomery, J. Ochterski and G. Petersson, *J. Chem. Phys.*, 1994, **101**, 5900–5909.

[38] G. Petersson and M. Allaham, *J. Chem. Phys.*, 1991, **94**, 6081–6090.

[39] G. Petersson, T. Tensfeldt and J. Montgomery, *J. Chem. Phys.*, 1991, **94**, 6091–6101.

[40] G. Petersson, A. Bennett, T. Tensfeldt, M. Allaham, W. Shirley and J. Mantzaris, *J. Chem. Phys.*, 1988, **89**, 2193–2218.

[41] M. Nyden and G. Petersson, *J. Chem. Phys.*, 1981, **75**, 1843–1862.

[42] K. A. Prather and Y. T. Lee, *Israel Journal of Chemistry*, 1994, **34**, 43–53.

[43] D. Price and E. Ratajczak, *J. Chem. Soc., Chem. Commun.*, 1976, **5**, 902–903.

[44] J. D. Chesko, D. Stranges, A. G. Suits and Y. T. Lee, *J. Chem. Phys.*, 1995, **103**, 405–422.

[45] M.-D. Su, *J. Phys. Chem. A*, 2006, **110**, 9420–9428.

[46] M.-F. Lin, Y. A. Dyakov, C.-M. Tseng, A. M. Mebel, S. H. Lin, Y. T. Lee and C.-K. Ni, *J. Chem. Phys*, 2006, **124**, 084303.

[47] C. S. Hansen, S. J. Blanksby, N. Chalyavi, E. J. Bieske, J. R. Reimers and A. J. Trevitt, *J. Chem. Phys.*, 2015, **142**, 014301.

[48] C. S. Hansen, B. B. Kirk, S. J. Blanksby and A. J. Trevitt, *J. Phys. Chem. A*, 2013, **117**, 10839–10846.

[49] I. Alata, J. Bert, M. Broquier, C. Dedonder, G. Feraud, G. Gregoire, S. Soorkia, E. Marceca and C. Jouvet, *The Journal of Physical Chemistry A*, 2013, **117**, 4420–4427.

[50] Y. Ranasinghe and G. Glish, *J. Am. Soc. Mass Spectrom.*, 1996, **7**, 473–481.

[51] M. Martin-Drumel, O. Pirali, Y. Loquais, C. Falvo and P. Brechignac, *Chem. Phys. Lett.*, 2013, **557**, 53 – 58.

[52] J. D. Bhawalkar, G. S. He and P. N. Prasad, *Rep. Prog. Phys.*, 1996, **59**, 1041.